This is a repository copy of *Finite element implementation of a multi-scale dynamic piezomagnetic continuum model*.

White Rose Research Online URL for this paper:
https://eprints.whiterose.ac.uk/164053/

Version: Accepted Version

Finite element implementation of a multi-scale dynamic piezomagnetic continuum model

Mingxiu Xu[1], Inna M. Gitman[2], Peijun Wei[1] and Harm Askes[3*]

[1]Department of Applied Mechanics, School of Mathematics and Physics,
University of Science and Technology Beijing, China

[2]Department of Mechanical Engineering,
The University of Sheffield, United Kingdom

[3]Department of Civil and Structural Engineering,
The University of Sheffield, United Kingdom

Abstract

A gradient-enriched dynamic piezomagnetic model is presented. The gradient enrichment introduces a number of microstructural terms in the model that allow the description of dispersive wave propagation. A novel derivation based on homogenisation principles is shown to lead to a multi-scale formulation in which the micro-scale displacements and magnetic potential are included alongside the macro-scale displacements and magnetic potential. The multi-scale formulation of the model has the significant advantage that all higher-order terms are rewritten as second-order spatial derivatives. As a consequence, a standard $\mathscr{C}^0$-continuous finite element discretisation can be used. Details of the finite element implementation are given. A series of one and two-dimensional examples shows the effectiveness of the model to describe dispersive wave propagation and remove singularities in a coupled elasto-magnetic context.

Keywords: piezomagnetism, wave propagation, generalised continuum, length scale, multiscale modelling, wave dispersion

1 Introduction

Exploring and exploiting the coupling between mechanical and magnetic material behaviour has led to innovation in various areas of technology, ranging from sensors and transducers to vibration dampers and valves. Many of these applications continue to be developed, often at smaller and smaller specimen sizes. To understand how the piezomagnetic coupling is affected by size, material models need to take into account how the microstructure of the material influences the macroscopic behaviour [29, 35, 36].

One approach to modelling is to incorporate the heterogeneity of the material within a multi-scale piezomagnetic framework. The different phases at the lower level of observation are modelled explicitly and homogenisation principles may be applied to derive effective properties [1, 2, 18, 27, 28]. This requires the identification of a suitable Representative Volume Element at the lower scale of observation, after which Fourier transforms [1, 2] or Eshelby solutions [18, 27, 28] may be used to quantify the relevant effective properties.

Alternatively, a more phenomenological approach is to enrich the governing piezomagnetic equations with additional terms that are envisaged to capture the microstructural effects. The theoretical framework

---

*corresponding author: h.askes@sheffield.ac.uk

of elasticity with couple stresses [42] and nonlocal elasticity [23] provides templates to formulate such generalised continua, whereby the additional terms typically are higher-order spatial derivatives of the standard terms, accompanied by one or more internal length scale parameters. Thus, piezomagnetic coupling has been combined with couple stress theory in [6] and the very similar [8], reporting increased apparent stiffness with increasing values of the internal length scale. On the other hand, Eringen-type nonlocality has been used in [9] where a decrease in apparent stiffness was reported for increasing values of the internal length scale, and in [19,37] where the equivalence of Eringen-type nonlocality with higher-order derivatives of accelerations was shown, thus explaining the apparent decrease in stiffness for increasing values of the length scale—see also [13] for the equivalence of stress gradients and inertia gradients. Naturally, it is also possible to have both types of enrichment in the same model [7,33], in which case there are two internal length scale parameters with competing effects on the apparent stiffness.

In addition, it is worthwhile to point out that the effects of magnetic field on the mechanical behaviour can be simulated by adding a magnetic force to the mechanical equations or by including the magnetic degrees of freedom alongside the mechanical degrees of freedom in an expanded set of equations. In the former approach, the mechanical response does not affect the magnetic response, whereas the latter approach is fully coupled. In the context of generalised continua, compare for instance [26] with [24].

However, since generalised continua models are equipped with higher-order spatial derivatives, numerical implementation typically requires continuity of the interpolation functions that is higher than the $\mathscr{C}^0$-continuity available in standard finite element packages. Achieving higher-order continuity is not straightforward but certainly possible, see [10] for an overview of methods and approaches. Aifantis suggested a series of models whereby the higher-order term is the Laplacian of the corresponding lower-order term [3–5]. With that particular mathematical structure of the equations, one of simplest methods of implementation is to rewrite the fourth-order differential equations of generalised elasticity into a set of second-order differential equations [15,32,39,41].

In this paper, we aim to bridge the gap between multi-scale models and generalised continua described above. We will explore homogenisation techniques that allow us to rewrite the equations of generalised piezomagnetic continua as a coupled set of multi-scale partial differential equations whereby the micro-scale mechanical and magnetic fields appear alongside the macro-scale mechanical and magnetic fields. This paper is the follow-up of earlier work we reported on statics [45] and a previous article where we explored suitable formats of gradient-enriched piezomagnetics in a one-dimensional dynamics context [44]. Novel aspects of the present paper include (i) a new motivation of the model that relies on homogenisation rather than postulation of an enriched energy functional, (ii) the extension to multiple spatial dimensions, (iii) the development of a simple $\mathscr{C}^0$-continuous finite element implementation, and (iv) the derivation of an optimal ratio of time step to element size. After briefly revisiting some relevant concepts of homogenisation in Section 2, a dynamic piezomagnetic model is formulated in Section 3—first as a generalised continuum model and subsequently as its multi-scale equivalent. The variationally consistent boundary conditions are derived in Section 4 and the finite element equations are given in Section 5. Section 6 presents an analysis of dispersive waves and compares the continuum with the space-time discretised equations; this enables the derivation of an optimal time step. The numerical examples of Section 7 demonstrate the convergence of the numerical model, the dispersive properties of the physical model and its ability to describe structural and material response without singularities.

2 Micro-macro transitions and gradient enrichment

In homogenisation procedures, the macro-level stresses σ_{ij}^{M} at a macro-level position $\mathbf{x^0}$ are found as the volume average of the micro-level stresses σ_{ij}^{m} through

$$\sigma_{ij}^{\mathrm{M}}(\mathbf{x^0}) = \frac{1}{V_{\mathrm{RVE}}} \int\limits_{V_{\mathrm{RVE}}} \sigma_{ij}^{\mathrm{m}}(\Delta\mathbf{x})\mathrm{d}\Omega \tag{1}$$

where $\Delta\mathbf{x} = \mathbf{x} - \mathbf{x^0}$. The integration volume is commonly known as the Representative Volume Element (RVE). Developing the micro-level stress in a Taylor series around its value at the centre $\mathbf{x^0}$ of the RVE

leads to

$$\sigma_{ij}^{\mathrm{M}}(\mathbf{x^0}) = \frac{1}{V_{\mathrm{RVE}}} \int\limits_{V_{\mathrm{RVE}}} \left(\sigma_{ij}^{\mathrm{m}}(\mathbf{x^0}) + \Delta x_k \sigma_{ij,k}^{\mathrm{m}}(\mathbf{x^0}) + \frac{1}{2}\Delta x_k \Delta x_l \sigma_{ij,kl}^{\mathrm{m}}(\mathbf{x^0}) + \dots \right) \mathrm{d}\Omega \tag{2}$$

where an index following a comma denotes a spatial partial derivative and the summation convention is implied. Noting that quantities evaluated at $\mathbf{x^0}$ are constant, the various integrals can be evaluated in terms of the RVE dimensions. For instance, taking a cubical RVE with lengths L_{RVE} yields

$$\sigma_{ij}^{\mathrm{M}} = \sigma_{ij}^{\mathrm{m}} + \frac{1}{24}L_{\mathrm{RVE}}^2 \sigma_{ij,kk}^{\mathrm{m}} + \mathcal{O}\left(L_{\mathrm{RVE}}^4\right) \tag{3}$$

where the $\mathbf{x^0}$-notation has been dropped. Following [38], we transform Eq. (3) by taking its second derivative, multiplying it with $\frac{1}{24}L_{\mathrm{RVE}}^2$ and substracting the result from the original Eq. (3). This gives

$$\sigma_{ij}^{\mathrm{M}} - \frac{1}{24}L_{\mathrm{RVE}}^2 \sigma_{ij,kk}^{\mathrm{M}} = \sigma_{ij}^{\mathrm{m}} + \mathcal{O}\left(L_{\mathrm{RVE}}^4\right) \tag{4}$$

Eqns. (3) and (4) are equivalent approximations of Eq. (1) upon truncation after the second-order term. These expressions demonstrate how micro-macro homogenisation schemes are related to gradient-enriched continuum models, which will be explored below in the context of piezomagnetic continua.

Remark 1 *Note that other assumptions on RVE shape or micro-macro transitions may lead to different numerical factors preceding the higher-order term in Eq. (4). Thus, a factor $\frac{1}{8}$ has been reported for a circular RVE [40]. Conversely, a factor $\frac{1}{12}$ was found for square RVEs with a second-order homogenisation scheme including higher-order stresses and higher-order strains [30] and square RVEs with a simultaneous perturbation of stiffness and strain terms [25]. However, in all cases the size of the RVE appears as an intrinsic length scale.*

3 Piezomagnetic field equations

Inspired by earlier work of Aifantis and coworkers in piezoelectric generalised continuum modelling [46], a static gradient-enriched piezomagnetic continuum model was proposed in [45] based on an energy density functional W written as

$$W = \frac{1}{2}C_{ijkl}\left(u_{i,j}u_{k,l} + \ell_1^2 u_{i,jm}u_{k,lm}\right) + q_{ijk}\left(u_{i,j}\phi_{,k} + \ell_2^2 u_{i,jm}\phi_{,km}\right) - \frac{1}{2}\mu_{ij}\left(\phi_{,i}\phi_{,j} + \ell_3^2\phi_{,im}\phi_{,jm}\right) \tag{5}$$

which leads to the following field equations:

$$C_{ijkl}\left(u_{k,jl} - \ell_1^2 u_{k,jlmm}\right) + q_{ijk}\left(\phi_{,jk} - \ell_2^2\phi_{,jkmm}\right) = 0 \tag{6a}$$

$$q_{ijk}\left(u_{i,jk} - \ell_2^2 u_{i,jkmm}\right) - \mu_{ij}\left(\phi_{,ij} - \ell_3^2\phi_{,ijmm}\right) = 0 \tag{6b}$$

The primary unknowns are the displacements u_i and the magnetic potential ϕ. Since no source term is included in Eq. (6b), a scalar magnetic potential ϕ has been adopted. The standard piezomagnetic material properties are contained in the elastic stiffness tensor C_{ijkl}, the piezomagnetic coupling tensor q_{ijk} and the magnetic permeability tensor μ_{ij}. In addition, the model contains three independent length scale parameters ℓ_1, ℓ_2 and ℓ_3 that incorporate the effects of material heterogeneity. The higher-order gradient terms associated with these length scales can be used to eliminate unwanted singularities from the mechanical strain $\varepsilon_{ij} = \frac{1}{2}\left(u_{i,j} + u_{j,i}\right)$ and magnetic field $H_i = -\phi_{,i}$ and to simulate the size-dependent piezomagnetic response of finite size specimens [45]. For $\ell_1 = \ell_2 = \ell_3 = 0$ a standard piezomagnetic continuum is obtained.

3.1 Transient piezomagnetic coupling

In [44] we explored one-dimensional dynamic extensions of the model given in Eqns. (6). The transient extension of Eqns. (6) in multiple spatial dimensions can be written as [12]

$$C_{ijkl}\left(u_{k,jl} - \ell_1^2 u_{k,jlmm}\right) + q_{ijk}\left(\phi_{,jk} - \ell_2^2 \phi_{,jkmm}\right) \quad = \quad \rho\left(\ddot{u}_i - \ell_4^2 \ddot{u}_{i,mm}\right) \tag{7a}$$

$$q_{ijk}\left(u_{i,jk} - \ell_2^2 u_{i,jkmm}\right) - \mu_{ij}\left(\phi_{,ij} - \ell_3^2 \phi_{,ijmm}\right) \quad = \quad -\mu^2 e\left(\ddot{\phi} - \ell_5^2 \ddot{\phi}_{,mm}\right) \tag{7b}$$

where ρ is the mass density and e is the electric permittivity. Two further length scales ℓ_4 and ℓ_5 have been included in order to model dispersive propagation of the piezomagnetic waves.

However, for practical applications it is appropriate to account for the difference between the propagation speed of mechanical signals and that of magnetic signals. These are roughly defined as the speed of sound and the speed of light, respectively, and they typically differ by many orders of magnitude. In this context, the magnetic response may be considered instantaneous compared to the mechanical response. This motivates the suppression of the right-hand-side of Eq. (7b) and, therefore, in this work we consider the combination of Eq. (7a) with Eq. (6b) to simulate transient piezomagnetic response.

3.2 Multi-scale formulation

Finite element discretisation of Eqns. (7a) and (6b) is complicated by the presence of the fourth-order spatial derivatives, which requires $\mathscr{C}^1$-continuity of the interpolants. We will use the format of Eq. (4) to rewrite the field equations such that $\mathscr{C}^0$-continuity of the interpolation suffices.

Inspection of Eqns. (7a) and (6b) shows two different length scales, ℓ_1 and ℓ_2, associated with the higher-order displacement derivatives. Similarly, the higher-order derivatives of the magnetic potential appear with length scales ℓ_2 and ℓ_3. Thermodynamic consistency dictates that, unless $\ell_1 = \ell_2 = \ell_3$, the two sets of higher-order derivatives of the displacements and magnetic potentials are accompanied by different coefficients—see Eq. (5). However, in the spirit of Section 2, it can be argued that the micro-macro relations should be based on unique length scale identifications, say

$$u_i^{\mathrm{M}} - \ell_1^2 u_{i,jj}^{\mathrm{M}} \quad = \quad u_i^{\mathrm{m}} \tag{8a}$$

$$\phi^{\mathrm{M}} - \ell_3^2 \phi_{,jj}^{\mathrm{M}} \quad = \quad \phi^{\mathrm{m}} \tag{8b}$$

where ℓ_1 and ℓ_3 are related to the Representative Volume Element sizes for the mechanical and the magnetic response, respectively. This requires setting $\ell_2 = \ell_1$ in Eq. (6b) but, at the same time, $\ell_2 = \ell_3$ in Eq. (7a). Although this clearly leads to a thermodynamic inconsistency in case $\ell_1 \neq \ell_3$, it will be shown below that this anomaly disappears in a multi-scale formulation.

Adopting all of the substitutions discussed above, Eqns. (7a) and (6b) are rewritten as

$$C_{ijkl} u_{k,jl}^{\mathrm{m}} + q_{ijk} \phi_{,jk}^{\mathrm{m}} \quad = \quad \rho\left(\ddot{u}_i^{\mathrm{M}} - \ell_4^2 \ddot{u}_{i,mm}^{\mathrm{M}}\right) \tag{9a}$$

$$q_{ijk} u_{i,jk}^{\mathrm{m}} - \mu_{ij} \phi_{,ij}^{\mathrm{m}} \quad = \quad 0 \tag{9b}$$

which are to be solved alongside Eqns. (8). Indeed, substituting Eqns. (8) into Eq. (9a) leads to Eq. (7a) with $\ell_2 = \ell_3$, whereas substituting Eqns. (8) into Eq. (9b) yields Eq. (6b) with $\ell_2 = \ell_1$. Thus, at this stage in the derivation, the model is still reducible to its fourth-order starting point.

A symmetric set of equations can be obtained following the procedure developed in [11]. The second time derivative of Eq. (8a) is taken to rewrite the right-hand-side of Eq. (9a) as

$$\rho\left(\ddot{u}_i^{\mathrm{M}} - \ell_4^2 \ddot{u}_{i,mm}^{\mathrm{M}}\right) = \rho\left(\ddot{u}_i^{\mathrm{M}} - \frac{\ell_4^2}{\ell_1^2}\left(\ddot{u}_i^{\mathrm{M}} - \ddot{u}_i^{\mathrm{m}}\right)\right) = \rho\left(\frac{\ell_4^2}{\ell_1^2}\ddot{u}_i^{\mathrm{m}} - \frac{\ell_4^2 - \ell_1^2}{\ell_1^2}\ddot{u}_i^{\mathrm{M}}\right) \tag{10}$$

In addition, Eq. (8a) is replaced by its acceleration format multiplied with $\rho(\ell_4^2 - \ell_1^2)/\ell_1^2$. Thus, the final format of the field equations reads

$$C_{ijkl} u_{k,jl}^{\mathrm{m}} + q_{ijk} \phi_{,jk}^{\mathrm{m}} = \rho\left(\frac{\ell_4^2}{\ell_1^2}\ddot{u}_i^{\mathrm{m}} - \frac{\ell_4^2 - \ell_1^2}{\ell_1^2}\ddot{u}_i^{\mathrm{M}}\right) \tag{11a}$$

4

$$0 = \rho \frac{\ell_4^2 - \ell_1^2}{\ell_1^2} \left(\ddot{u}_i^{\mathrm{M}} - \ddot{u}_i^{\mathrm{m}} - \ell_1^2 \ddot{u}_{i,mm}^{\mathrm{M}} \right) \tag{11b}$$

$$q_{ijk} u_{i,jk}^{\mathrm{m}} - \mu_{ij} \phi_{,ij}^{\mathrm{m}} = 0 \tag{11c}$$

$$\phi^{\mathrm{M}} - \ell_3^2 \phi_{,jj}^{\mathrm{M}} = \phi^{\mathrm{m}} \tag{11d}$$

Since Eq. (8a) has been replaced by its acceleration counterpart Eq. (11b), the model equations are now no longer reducible to their fourth-order starting point. Instead, Eqns. (11) represent a new model whereby the mechanical gradient effects are incorporated in the transient terms only.

Note that Eqns. (11a–11c) are coupled, whereas Eq. (11d) is decoupled. This implies Eqns. (11a–11c) can be solved for u_i^{m}, u_i^{M} and ϕ^{m}, after which the micro-scale magnetic potential ϕ^{m} can be used as a source term in Eq. (11d) to solve for the macro-scale magnetic potential ϕ^{M}. Furthermore, it is noted that Eqns. (11a–11c) are symmetric: the coefficients of u_i^{M} in Eq. (11a) and u_i^{m} in Eq. (11b) match, as do the coefficients of ϕ^{m} in Eq. (11a) and u_i^{m} in Eq. (11c). This facilitates the identification of an associated energy functional, as will be shown in Section 4. Thus, the thermodynamic inconsistency discussed above is no longer present, which is the consequence of replacing Eq. (8a) with its second time derivative.

4 Variational formulation and boundary conditions

The Lagrangian density $\mathscr{L}$ underlying Eqns. (11a–11c) reads

$$
\begin{aligned}
\mathscr{L} = {} & \frac{1}{2}\rho \left((\dot{u}_i^{\mathrm{m}})^2 + \frac{\ell_4^2 - \ell_1^2}{\ell_1^2} \left(\dot{u}_i^{\mathrm{m}} - \dot{u}_i^{\mathrm{M}} \right)^2 + \left(\ell_4^2 - \ell_1^2 \right) \left(\dot{u}_{i,j}^{\mathrm{M}} \right)^2 \right) \\
& - \frac{1}{2} C_{ijkl} u_{i,j}^{\mathrm{m}} u_{k,l}^{\mathrm{m}} - q_{ijk} u_{i,j}^{\mathrm{m}} \phi_{,k}^{\mathrm{m}} + \frac{1}{2} \mu_{ij} \phi_{,i}^{\mathrm{m}} \phi_{,j}^{\mathrm{m}}
\end{aligned}
\tag{12}
$$

so that the Lagrangian L can be written as

$$
L = \int\limits_V \int\limits_{t_0}^{t_1} \mathscr{L} \, \mathrm{d}t \mathrm{d}\Omega + \int\limits_{S_n} \int\limits_{t_0}^{t_1} \left(u_i^{\mathrm{m}} f_i + \phi^{\mathrm{m}} g \right) \mathrm{d}t \mathrm{d}\Gamma
\tag{13}
$$

where f_i and g are prescribed values of mechanical tractions and magnetic flux, respectively. Furthermore, S_n and S_e are the parts of the boundary S of the domain V where natural and essential boundary conditions are applied, respectively, such that $S = S_n \cup S_e$ and $\emptyset = S_n \cap S_e$.

Requiring stationarity of L yields

$$
\delta L = \int\limits_V \int\limits_{t_0}^{t_1} \left(\delta \dot{u}_i^{\mathrm{m}} \frac{\partial \mathscr{L}}{\partial \dot{u}_i^{\mathrm{m}}} + \delta \dot{u}_i^{\mathrm{M}} \frac{\partial \mathscr{L}}{\partial \dot{u}_i^{\mathrm{M}}} + \delta \dot{u}_{i,j}^{\mathrm{M}} \frac{\partial \mathscr{L}}{\partial \dot{u}_{i,j}^{\mathrm{M}}} + \delta u_{i,j}^{\mathrm{m}} \frac{\partial \mathscr{L}}{\partial u_{i,j}^{\mathrm{m}}} + \delta \phi_{,i}^{\mathrm{m}} \frac{\partial \mathscr{L}}{\partial \phi_{,i}^{\mathrm{m}}} \right) \mathrm{d}t \mathrm{d}\Omega = 0
\tag{14}
$$

Integration by parts then leads to

$$
\begin{aligned}
& - \int\limits_V \int\limits_{t_0}^{t_1} \delta u_i^{\mathrm{m}} \left(\frac{\partial}{\partial t} \frac{\partial \mathscr{L}}{\partial \dot{u}_i^{\mathrm{m}}} + \frac{\partial}{\partial x_j} \frac{\partial \mathscr{L}}{\partial u_{i,j}^{\mathrm{m}}} \right) \mathrm{d}t \mathrm{d}\Omega + \int\limits_V \left[\delta u_i^{\mathrm{m}} \frac{\partial \mathscr{L}}{\partial \dot{u}_i^{\mathrm{m}}} \right]_{t_0}^{t_1} \mathrm{d}\Omega + \int\limits_{S_n} \int\limits_{t_0}^{t_1} \delta u_i^{\mathrm{m}} \left(n_j \frac{\partial \mathscr{L}}{\partial u_{i,j}^{\mathrm{m}}} + f_i \right) \mathrm{d}t \mathrm{d}\Gamma \\
& - \int\limits_V \int\limits_{t_0}^{t_1} \delta u_i^{\mathrm{M}} \left(\frac{\partial}{\partial t} \frac{\partial \mathscr{L}}{\partial \dot{u}_i^{\mathrm{M}}} - \frac{\partial^2}{\partial x_j \partial t} \frac{\partial \mathscr{L}}{\partial \dot{u}_{i,j}^{\mathrm{M}}} \right) \mathrm{d}t \mathrm{d}\Omega + \int\limits_V \left[\delta u_i^{\mathrm{M}} \frac{\partial \mathscr{L}}{\partial \dot{u}_i^{\mathrm{M}}} \right]_{t_0}^{t_1} \mathrm{d}\Omega + \int\limits_V \left[\delta u_{i,j}^{\mathrm{M}} \frac{\partial \mathscr{L}}{\partial \dot{u}_{i,j}^{\mathrm{M}}} \right]_{t_0}^{t_1} \mathrm{d}\Omega \\
& - \int\limits_{S_n} \int\limits_{t_0}^{t_1} \delta u_i^{\mathrm{M}} n_j \frac{\partial}{\partial t} \frac{\partial \mathscr{L}}{\partial \dot{u}_{i,j}^{\mathrm{M}}} \mathrm{d}t \mathrm{d}\Gamma - \int\limits_V \int\limits_{t_0}^{t_1} \delta \phi^{\mathrm{m}} \frac{\partial}{\partial x_i} \frac{\partial \mathscr{L}}{\partial \phi_{,i}^{\mathrm{m}}} \mathrm{d}t \mathrm{d}\Omega + \int\limits_{S_n} \int\limits_{t_0}^{t_1} \delta \phi^{\mathrm{m}} \left(n_i \frac{\partial \mathscr{L}}{\partial \phi_{,i}^{\mathrm{m}}} + g \right) \mathrm{d}t \mathrm{d}\Gamma = 0
\end{aligned}
\tag{15}
$$

where n_j is the outward normal to the boundary S. Assuming the response of the system is known at the start and end of the analysis, the second, fifth and sixth integral in Eq. (15) cancel. The remaining integrals have to vanish individually; it can be verified that the first, fourth and eighth lead to the field equations given earlier in Eqns. (11a–11c). The associated boundary conditions are

$$\text{either} \quad u_i^{\mathrm{m}} \text{ prescribed} \quad \text{or} \quad n_j \left(C_{ijkl} u_{k,l}^{\mathrm{m}} + q_{ijk} \phi_{,k}^{\mathrm{m}} \right) = f_i \tag{16a}$$

$$\text{either} \quad u_i^{\mathrm{M}} \text{ prescribed} \quad \text{or} \quad n_j \rho \left(\ell_4^2 - \ell_1^2 \right) \ddot{u}_{i,j}^{\mathrm{M}} = 0 \tag{16b}$$

$$\text{either} \quad \phi^{\mathrm{m}} \text{ prescribed} \quad \text{or} \quad n_k \left(q_{ijk} u_{i,j}^{\mathrm{m}} - \mu_{ik} \phi_{,i}^{\mathrm{m}} \right) = g \tag{16c}$$

Through the natural boundary conditions of Eqns. (16a) and (16c) the standard definitions of stress σ_{ij} and magnetic flux density B_k in a piezomagnetic medium are retrieved:

$$\sigma_{ij}^{\mathrm{m}} = C_{ijkl} \varepsilon_{kl}^{\mathrm{m}} - q_{ijk} H_k^{\mathrm{m}} = C_{ijkl} u_{k,l}^{\mathrm{m}} + q_{ijk} \phi_{,k}^{\mathrm{m}} \tag{17a}$$

$$B_k^{\mathrm{m}} = q_{ijk} \varepsilon_{ij}^{\mathrm{m}} + \mu_{ik} H_i^{\mathrm{m}} = q_{ijk} u_{i,j}^{\mathrm{m}} - \mu_{ik} \phi_{,i}^{\mathrm{m}} \tag{17b}$$

However, the meaning of the natural boundary condition of Eq. (16b) is less clear. From dimensional analysis, it follows that this concerns a stress-type quantity, but it is asymmetric and proportional to the macro-level acceleration field. The occurrence of non-standard boundary conditions is common when dealing with gradient-enriched continuum models, and as yet there is no firm consensus on a preferred format. In an earlier one-dimensional study it was suggested to tie the macro-scale and micro-scale displacements on the boundary [14]. This could be interpreted as volume preservation and in a multi-dimensional context it can be applied to the normal components of the two displacement fields on the boundary. This will be explored below.

5 Finite element discretisation

The continuum equations (11a–11d) are decoupled, in that the macro-scale magnetic potential does not appear in Eqns. (11a–11c). Thus, Eq. (11d) can be solved separately from Eqns. (11a–11c), and the associated finite element equations are treated separately below. Throughout this Section, we will adopt standard Voigt notation.

5.1 Transient piezomagnetic equations

The transient piezomagnetic field equations (11a–11c) are written in a weak form as

$$\int_V (\delta \mathbf{u}^{\mathrm{m}})^T \rho \left(\frac{\ell_4^2}{\ell_1^2} \ddot{\mathbf{u}}^{\mathrm{m}} - \frac{\ell_4^2 - \ell_1^2}{\ell_1^2} \ddot{\mathbf{u}}^{\mathrm{M}} \right) \mathrm{d}\Omega - \int_V (\delta \mathbf{u}^{\mathrm{m}})^T \mathbf{L}^T \left(\mathbf{C} \mathbf{L} \mathbf{u}^{\mathrm{m}} + \mathbf{Q} \nabla \boldsymbol{\phi}^{\mathrm{m}} \right) \mathrm{d}\Omega = 0 \tag{18a}$$

$$\int_V \left(\delta \mathbf{u}^{\mathrm{M}} \right)^T \rho \frac{\ell_4^2 - \ell_1^2}{\ell_1^2} \left(-\ddot{\mathbf{u}}^{\mathrm{m}} + \ddot{\mathbf{u}}^{\mathrm{M}} - \ell_1^2 \nabla^2 \ddot{\mathbf{u}}^{\mathrm{M}} \right) \mathrm{d}\Omega = 0 \tag{18b}$$

$$-\int_V \delta \boldsymbol{\phi}^{\mathrm{m}} \nabla^T \left(\mathbf{Q}^T \mathbf{L} \mathbf{u}^{\mathrm{m}} - \mathbf{P} \nabla \boldsymbol{\phi}^{\mathrm{m}} \right) \mathrm{d}\Omega = 0 \tag{18c}$$

where $\mathbf{C}$, $\mathbf{Q}$ and $\mathbf{P}$ are the matrix equivalents of C_{ijkl}, q_{ijk} and μ_{ij}, respectively, $\mathbf{L}$ is the usual strain-displacement differential operator, and $\nabla^2 = \nabla^T \nabla$. Furthermore, $\delta \mathbf{u}^{\mathrm{m}}$, $\delta \mathbf{u}^{\mathrm{M}}$ and $\delta \boldsymbol{\phi}^{\mathrm{m}}$ are test functions associated with $\mathbf{u}^{\mathrm{m}}$, $\mathbf{u}^{\mathrm{M}}$ and $\boldsymbol{\phi}^{\mathrm{m}}$, respectively. Integration by parts and substitution of the natural boundary

conditions defined in Eqns. (16) then yields

$$\int_V (\delta \mathbf{u}^{\mathrm{m}})^T \rho \left(\frac{\ell_4^2}{\ell_1^2} \ddot{\mathbf{u}}^{\mathrm{m}} - \frac{\ell_4^2 - \ell_1^2}{\ell_1^2} \ddot{\mathbf{u}}^{\mathrm{M}} \right) \mathrm{d}\Omega + \int_V (\mathbf{L}\delta \mathbf{u}^{\mathrm{m}})^T (\mathbf{C}\mathbf{L}\mathbf{u}^{\mathrm{m}} + \mathbf{Q}\nabla \boldsymbol{\phi}^{\mathrm{m}}) \, \mathrm{d}\Omega \quad = \quad \int_{S_n} (\delta \mathbf{u}^{\mathrm{m}})^T \mathbf{f} \, \mathrm{d}\Gamma \tag{19a}$$

$$\int_V (\delta \mathbf{u}^{\mathrm{M}})^T \rho \frac{\ell_4^2 - \ell_1^2}{\ell_1^2} \left(-\ddot{\mathbf{u}}^{\mathrm{m}} + \ddot{\mathbf{u}}^{\mathrm{M}} \right) \mathrm{d}\Omega + \int_V (\nabla \delta \mathbf{u}^{\mathrm{M}})^T \rho \left(\ell_4^2 - \ell_1^2 \right) \nabla \ddot{\mathbf{u}}^{\mathrm{M}} \mathrm{d}\Omega \quad = \quad 0 \tag{19b}$$

$$\int_V (\nabla \delta \boldsymbol{\phi}^{\mathrm{m}})^T \left(\mathbf{Q}^T \mathbf{L} \mathbf{u}^{\mathrm{m}} - \mathbf{P}\nabla \boldsymbol{\phi}^{\mathrm{m}} \right) \mathrm{d}\Omega \quad = \quad \int_{S_n} \delta \boldsymbol{\phi}^{\mathrm{m}} \mathbf{g} \, \mathrm{d}\Gamma \tag{19c}$$

Next, the various continuous fields (displacements, magnetic potentials and the associated test functions) are discretised with finite element shape functions. For simplicity, we will use the same shape functions for all fields, that is

$$\mathbf{u}^{\mathrm{m}} \approx \begin{bmatrix} N_1 & 0 & 0 & N_2 & 0 & 0 & \dots \\ 0 & N_1 & 0 & 0 & N_2 & 0 & \dots \\ 0 & 0 & N_1 & 0 & 0 & N_2 & \dots \end{bmatrix} \mathbf{d}^{\mathrm{m}} \equiv \mathbf{N_u} \mathbf{d}^{\mathrm{m}} \tag{20a}$$

$$\boldsymbol{\phi}^{\mathrm{m}} \approx \begin{bmatrix} N_1 & N_2 & \dots \end{bmatrix} \boldsymbol{\psi}^{\mathrm{m}} \equiv \mathbf{N_\phi} \boldsymbol{\psi}^{\mathrm{m}} \tag{20b}$$

and so forth. This leads to the following set of semi-discretised equations:

$$\begin{bmatrix} \mathbf{M}_{uu}^{mm} & \mathbf{M}_{uu}^{mM} & 0 \\ \mathbf{M}_{uu}^{Mm} & \mathbf{M}_{uu}^{MM} & 0 \\ 0 & 0 & 0 \end{bmatrix} \begin{bmatrix} \ddot{\mathbf{d}}^{\mathrm{m}} \\ \ddot{\mathbf{d}}^{\mathrm{M}} \\ \ddot{\boldsymbol{\psi}}^{\mathrm{m}} \end{bmatrix} + \begin{bmatrix} \mathbf{K}_{uu}^{mm} & 0 & \mathbf{K}_{u\phi}^{mm} \\ 0 & 0 & 0 \\ \mathbf{K}_{\phi u}^{mm} & 0 & \mathbf{K}_{\phi\phi}^{mm} \end{bmatrix} \begin{bmatrix} \mathbf{d}^{\mathrm{m}} \\ \mathbf{d}^{\mathrm{M}} \\ \boldsymbol{\psi}^{\mathrm{m}} \end{bmatrix} = \begin{bmatrix} \mathbf{F} \\ 0 \\ \mathbf{G} \end{bmatrix} \tag{21}$$

where $\mathbf{d}^{\mathrm{m}}$, $\mathbf{d}^{\mathrm{M}}$ and $\boldsymbol{\psi}^{\mathrm{m}}$ contain the nodal values of micro-scale displacements, macro-scale displacements and micro-scale magnetic potentials, respectively. Furthermore,

$$\mathbf{M}_{uu}^{mm} = \int_V \mathbf{N}_u^T \rho \frac{\ell_4^2}{\ell_1^2} \mathbf{N}_u \mathrm{d}\Omega \tag{22a}$$

$$\mathbf{M}_{uu}^{mM} = \left(\mathbf{M}_{uu}^{Mm} \right)^T = -\int_V \mathbf{N}_u^T \rho \frac{\ell_4^2 - \ell_1^2}{\ell_1^2} \mathbf{N}_u \mathrm{d}\Omega \tag{22b}$$

$$\mathbf{M}_{uu}^{MM} = \int_V \mathbf{N}_u^T \rho \frac{\ell_4^2 - \ell_1^2}{\ell_1^2} \mathbf{N}_u \mathrm{d}\Omega + \int_V \sum_{\xi=x,y,z} \frac{\partial \mathbf{N}_u^T}{\partial \xi} \rho \left(\ell_4^2 - \ell_1^2 \right) \frac{\partial \mathbf{N}_u}{\partial \xi} \mathrm{d}\Omega \tag{22c}$$

$$\mathbf{K}_{uu}^{mm} = \int_V \mathbf{B}_u^T \mathbf{C} \mathbf{B}_u \mathrm{d}\Omega \tag{22d}$$

$$\mathbf{K}_{u\phi}^{mm} = \mathbf{K}_{\phi u}^{T} = \int_V \mathbf{B}_u^T \mathbf{Q} \mathbf{B}_\phi \mathrm{d}\Omega \tag{22e}$$

$$\mathbf{K}_{\phi\phi}^{mm} = -\int_V \mathbf{B}_\phi^T \mathbf{P} \mathbf{B}_\phi \mathrm{d}\Omega \tag{22f}$$

with $\mathbf{B}_u = \mathbf{L}\mathbf{N}_u$ and $\mathbf{B}_\phi = \nabla \mathbf{N}_\phi$. The vectors $\mathbf{F}$ and $\mathbf{G}$ contain the driving mechanical and magnetic nodal forces, respectively. The structure of Eq. (21) highlights how the multi-scale coupling is separated from the coupled physics: the former is included in the transient terms, and the latter in the quasi-static terms. This,

in turn, allows for straightforward static condensation of the magnetic degrees of freedom. That is, Eq. (21) can be recast as

$$
\begin{bmatrix} \mathbf{M}_{\mathrm{uu}}^{\mathrm{mm}} & \mathbf{M}_{\mathrm{uu}}^{\mathrm{mM}} \\ \mathbf{M}_{\mathrm{uu}}^{\mathrm{Mm}} & \mathbf{M}_{\mathrm{uu}}^{\mathrm{MM}} \end{bmatrix} \begin{bmatrix} \ddot{\mathbf{d}}^{\mathrm{m}} \\ \ddot{\mathbf{d}}^{\mathrm{M}} \end{bmatrix} + \begin{bmatrix} \mathbf{K}_{\mathrm{uu}}^{\mathrm{mm}} - \mathbf{K}_{\mathrm{u}\phi}^{\mathrm{mm}} \left(\mathbf{K}_{\phi\phi}^{\mathrm{mm}} \right)^{-1} \mathbf{K}_{\phi\mathrm{u}}^{\mathrm{mm}} & 0 \\ 0 & 0 \end{bmatrix} \begin{bmatrix} \mathbf{d}^{\mathrm{m}} \\ \mathbf{d}^{\mathrm{M}} \end{bmatrix}
$$

$$
= \begin{bmatrix} \mathbf{F} - \mathbf{K}_{\mathrm{u}\phi}^{\mathrm{mm}} \left(\mathbf{K}_{\phi\phi}^{\mathrm{mm}} \right)^{-1} \mathbf{G} \\ 0 \end{bmatrix} \tag{23}
$$

which improves the condition number of the resulting system matrix. Further condensation is possible by eliminating the macro-scale displacements using the second row of Eq. (23), but this has not been explored here.

Remark 2 *Separating the gradient enrichment (included in the mass matrix) from the constitutive behaviour (included in the stiffness matrix) provides a template for the extension towards nonlinear material behaviour. Gradient-enriched plasticity and/or damage can then be incorporated via straightforward additions to the stiffness matrix to simulate mesh-independent failure zones [17].*

5.2 Multi-scale postprocessing of the magnetic potential

The multi-scale coupling of magnetic potential is decoupled from the transient piezomagnetic response. The weak form of Eq. (11d) reads

$$
\int_V \delta \boldsymbol{\phi}^{\mathrm{M}} \left(\boldsymbol{\phi}^{\mathrm{M}} - \ell_3^2 \nabla^2 \boldsymbol{\phi}^{\mathrm{M}} \right) \mathrm{d}\Omega = \int_V \delta \boldsymbol{\phi}^{\mathrm{M}} \boldsymbol{\phi}^{\mathrm{m}} \mathrm{d}\Omega \tag{24}
$$

where $\delta \boldsymbol{\phi}^{\mathrm{M}}$ is an appropriate test function. Integration by parts results in

$$
\int_V \delta \boldsymbol{\phi}^{\mathrm{M}} \boldsymbol{\phi}^{\mathrm{M}} \, \mathrm{d}\Omega + \int_V \left(\nabla \delta \boldsymbol{\phi}^{\mathrm{M}} \right)^T \ell_3^2 \nabla \boldsymbol{\phi}^{\mathrm{M}} \mathrm{d}\Omega = \int_V \delta \boldsymbol{\phi}^{\mathrm{M}} \boldsymbol{\phi}^{\mathrm{m}} \mathrm{d}\Omega + \oint_S \delta \boldsymbol{\phi}^{\mathrm{M}} \, \mathbf{n}^T \nabla \boldsymbol{\phi}^{\mathrm{M}} \mathrm{d}\Gamma \tag{25}
$$

The boundary integral will cancel by assuming essential boundary conditions (via tyings between the micro and macro-scale displacements) or homogeneous natural boundary conditions (in the absence of said tyings). Finite element discretisation is applied with the same set of shape functions as above, that is $\boldsymbol{\phi}^{\mathrm{M}} \approx \mathbf{N}_\phi \boldsymbol{\psi}^{\mathrm{M}}$ and $\delta \boldsymbol{\phi}^{\mathrm{M}} \approx \mathbf{N}_\phi \delta \boldsymbol{\psi}^{\mathrm{M}}$. This leads to the following system of equations:

$$
\left[\int_V \mathbf{N}_\phi^T \mathbf{N}_\phi \mathrm{d}\Omega + \int_V \sum_{\xi = x,y,z} \frac{\partial \mathbf{N}_\phi^T}{\partial \xi} \ell_3^2 \frac{\partial \mathbf{N}_\phi}{\partial \xi} \mathrm{d}\Omega \right] \boldsymbol{\psi}^{\mathrm{M}} = \int_V \mathbf{N}_\phi^T \mathbf{N}_\phi \mathrm{d}\Omega \, \boldsymbol{\psi}^{\mathrm{m}} \tag{26}
$$

which can be solved for $\boldsymbol{\psi}^{\mathrm{M}}$ using values for $\boldsymbol{\psi}^{\mathrm{m}} = \left(\mathbf{K}_{\phi\phi}^{\mathrm{mm}} \right)^{-1} \left(\mathbf{G} - \mathbf{K}_{\phi\mathrm{u}}^{\mathrm{mm}} \mathbf{d}^{\mathrm{m}} \right)$ as source term. There are no transient terms present in Eq. (26), thus there is no strict need to solve Eq. (26) at every time instant. In fact, Eq. (26) serves as a multi-scale postprocessing step that can be invoked as and when required by the user.

6 Dispersion analysis

In a transient time-domain simulation, the temporal and spatial resolutions must be balanced. It makes little sense to combine a small time step with a coarse finite element mesh, and vice versa. For the one-dimensional version of the numerical model of Eq. (21) it is possible to find an estimate for an optimal ratio between time step size and element size by comparing the dispersion relation of the discretised equations with the dispersion relation of the continuum. This analysis extends earlier work in gradient elasticity with first-order [16] and second-order [21] micro-inertia to coupled physics in Section 6.2; it also provides a newly derived closed-form expression for the estimated optimal time step in Section 6.3.
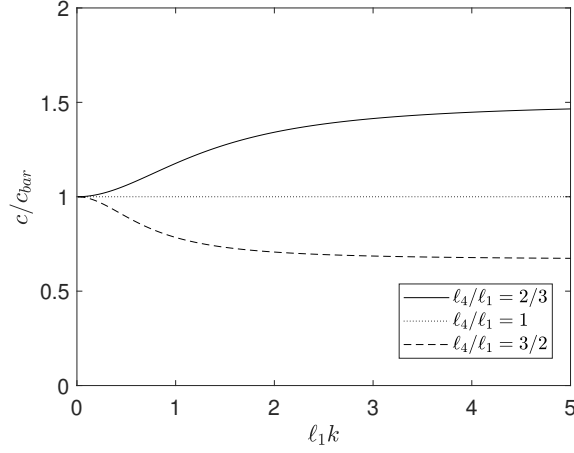
Figure 1: Dispersion analysis: normalised phase velocity against normalised wave number

6.1 Dispersion relation of the continuum

With only one spatial coordinate, Eq. (11c) can be used to eliminate the micro-scale magnetic potential from Eq. (11a), so that Eqns. (11a) and (11b) are a coupled set of equations with unknowns u_x^{m} and u_x^{M}. Assuming an infinitely long medium, we substitute the following trial solutions:

$$u_x^{\mathrm{m}} = U^{\mathrm{m}} \exp\left(\mathrm{i}k\left(x - ct\right)\right) \tag{27a}$$
$$u_x^{\mathrm{M}} = U^{\mathrm{M}} \exp\left(\mathrm{i}k\left(x - ct\right)\right) \tag{27b}$$

where k is the wave number, c is the phase velocity, and U^{m} and U^{M} are the amplitudes. This gives

$$\left(E + \frac{q^2}{\mu}\right) U^{\mathrm{m}} = \rho c^2 \left(\frac{\ell_4^2}{\ell_1^2} U^{\mathrm{m}} - \frac{\ell_4^2 - \ell_1^2}{\ell_1^2} U^{\mathrm{M}}\right) \tag{28a}$$

$$0 = U^{\mathrm{M}} \left(1 + \ell_1^2 k^2\right) - U^{\mathrm{m}} \tag{28b}$$

with E the Young's modulus. Elimination of the two amplitudes leads to

$$\frac{c^2}{c_{\mathrm{bar}}^2} = \frac{1 + \ell_1^2 k^2}{1 + \ell_4^2 k^2} \tag{29}$$

where

$$c_{\mathrm{bar}} = \sqrt{\frac{E}{\rho} + \frac{q^2}{\mu\rho}} \tag{30}$$

is the longitudinal propagation velocity of a signal in a standard (i.e. without gradient enrichment) medium. For $\ell_1 = \ell_4 = 0$, and indeed for $\ell_1 = \ell_4 \neq 0$, the phase velocity c does not depend on the wave number k. For such cases, the medium is non-dispersive. Conversely, taking $\ell_1 \neq \ell_4$ yields $c = c(k)$ which means that the different harmonic components of a signal travel with different propagation velocities. In Figure 1 we have plotted the phase velocity against the wave number for a range of values of ℓ_4/ℓ_1, which aids to verify that $c/c_{\mathrm{bar}} \to \ell_1/\ell_4$ for $k \to \infty$.

A more in-depth dispersion analysis, including a comparison with the equivalent mono-scale model, can be found in [44]. The purpose here is to compare the dispersion relation of the continuum with that of the discretised equations.

9

6.2 Dispersion relation of the discretised equations

Assuming a uniform one-dimensional finite element mesh consisting of linear elements of length h, the use of a consistent mass matrix, and the absence of external loads, the second row of Eq. (21) reads

$$-\rho h \frac{\ell_4^2 - \ell_1^2}{\ell_1^2} \left(\tfrac{1}{6}\ddot{d}_{j,n-1}^{\mathrm{m}} + \tfrac{2}{3}\ddot{d}_{j,n}^{\mathrm{m}} + \tfrac{1}{6}\ddot{d}_{j,n+1}^{\mathrm{m}} \right) + \rho h \frac{\ell_4^2 - \ell_1^2}{\ell_1^2} \left(\tfrac{1}{6}\ddot{d}_{j,n-1}^{\mathrm{M}} + \tfrac{2}{3}\ddot{d}_{j,n}^{\mathrm{M}} + \tfrac{1}{6}\ddot{d}_{j,n+1}^{\mathrm{M}} \right)$$
$$+ \frac{\rho}{h} \left(\ell_4^2 - \ell_1^2 \right) \left(-\ddot{d}_{j,n-1}^{\mathrm{M}} + 2\ddot{d}_{j,n}^{\mathrm{M}} - \ddot{d}_{j,n+1}^{\mathrm{M}} \right) \quad = \quad 0 \qquad (31)$$

where a subscript j indicates the time instant and a subscript n represents the node number. The trial solutions are written as

$$\ddot{d}_{j,n}^{\mathrm{m}} = D^{\mathrm{m}} \exp\left(\mathrm{i}k\left(x_n - ct_j \right) \right) = D^{\mathrm{m}} \exp\left(\mathrm{i}k\left(nh - cj\Delta t \right) \right) \qquad (32a)$$

$$\ddot{d}_{j,n}^{\mathrm{M}} = D^{\mathrm{M}} \exp\left(\mathrm{i}k\left(x_n - ct_j \right) \right) = D^{\mathrm{M}} \exp\left(\mathrm{i}k\left(nh - cj\Delta t \right) \right) \qquad (32b)$$

where D^{m} and D^{M} are amplitudes, so that $\ddot{d}_{j,n\pm1} = \ddot{d}_{j,n}\exp\left(\pm\mathrm{i}kh\right)$. Substituting these trial solutions into Eq. (31) leads to

$$-\rho h \frac{\ell_4^2 - \ell_1^2}{\ell_1^2} D^{\mathrm{m}} \left(\tfrac{1}{6}\exp\left(-\mathrm{i}kh\right) + \tfrac{2}{3} + \tfrac{1}{6}\exp\left(\mathrm{i}kh\right) \right)$$
$$+\rho h \frac{\ell_4^2 - \ell_1^2}{\ell_1^2} D^{\mathrm{M}} \left(\tfrac{1}{6}\exp\left(-\mathrm{i}kh\right) + \tfrac{2}{3} + \tfrac{1}{6}\exp\left(\mathrm{i}kh\right) \right)$$
$$+\frac{\rho}{h} \left(\ell_4^2 - \ell_1^2 \right) D^{\mathrm{M}} \left(-\exp\left(-\mathrm{i}kh\right) + 2 - \exp\left(\mathrm{i}kh\right) \right) \quad = \quad 0 \qquad (33)$$

so that

$$\frac{D^{\mathrm{m}}}{D^{\mathrm{M}}} = \frac{\tfrac{2}{3} + \tfrac{1}{3}\cos(kh) + \dfrac{2\ell_1^2}{h^2}\left(1 - \cos(kh)\right)}{\tfrac{2}{3} + \tfrac{1}{3}\cos(kh)} \qquad (34)$$

which provides a first relation between the two amplitudes.

Deriving a second relation between D^{m} and D^{M} involves a few additional steps, namely writing the micro-scale magnetic potentials in terms of the micro-scale displacements and, subsequently, writing the micro-scale displacements in terms of micro-scale accelerations. Firstly, the third row of Eq. (21) can be written as

$$\frac{q}{h} \left(-d_{j,n-1}^{\mathrm{m}} + 2d_{j,n}^{\mathrm{m}} - d_{j,n+1}^{\mathrm{m}} \right) - \frac{\mu}{h} \left(-\psi_{j,n-1}^{\mathrm{m}} + 2\psi_{j,n}^{\mathrm{m}} - \psi_{j,n+1}^{\mathrm{m}} \right) = 0 \qquad (35)$$

This can be used to eliminate the nodal magnetic potentials from the first row of Eq. (21), namely

$$\rho h \frac{\ell_4^2}{\ell_1^2} \left(\tfrac{1}{6}\ddot{d}_{j,n-1}^{\mathrm{m}} + \tfrac{2}{3}\ddot{d}_{j,n}^{\mathrm{m}} + \tfrac{1}{6}\ddot{d}_{j,n+1}^{\mathrm{m}} \right) - \rho h \frac{\ell_4^2 - \ell_1^2}{\ell_1^2} \left(\tfrac{1}{6}\ddot{d}_{j,n-1}^{\mathrm{M}} + \tfrac{2}{3}\ddot{d}_{j,n}^{\mathrm{M}} + \tfrac{1}{6}\ddot{d}_{j,n+1}^{\mathrm{M}} \right)$$
$$+ \left(\frac{E}{h} + \frac{q^2}{\mu h} \right) \left(-d_{j,n-1}^{\mathrm{m}} + 2d_{j,n}^{\mathrm{m}} - d_{j,n+1}^{\mathrm{m}} \right) \quad = \quad 0 \qquad (36)$$

Next, we will use Eq. (54) derived in Appendix A to rewrite the micro-scale displacements in terms of micro-scale accelerations. To apply Eq. (54), it is necessary to evaluate Eq. (36) at three successive time instants t_{j-1}, t_j and t_{j+1}. Following the structure of Eq. (54), these three evaluations of Eq. (36) are weighted
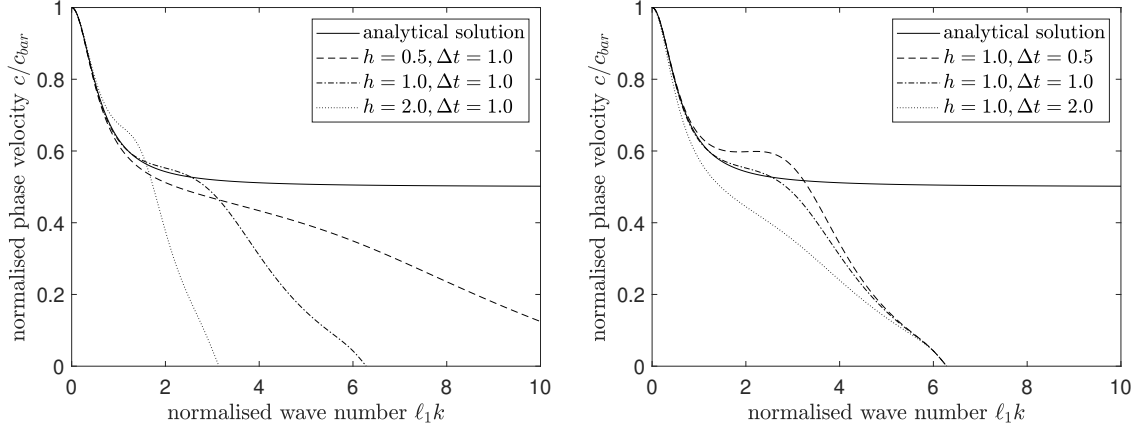
10

Figure 2: Discrete versus analytical dispersion curves: variation of element size (left) and time step (right)

with factors -1, 2 and -1, respectively, and added together. This results in

$$\rho h \frac{\ell_4^2}{\ell_1^2} \left(-\tfrac{1}{6}\ddot{d}_{j-1,n-1}^{m} - \tfrac{2}{3}\ddot{d}_{j-1,n}^{m} - \tfrac{1}{6}\ddot{d}_{j-1,n+1}^{m} + \tfrac{1}{3}\ddot{d}_{j,n-1}^{m} + \tfrac{4}{3}\ddot{d}_{j,n}^{m} + \tfrac{1}{3}\ddot{d}_{j,n+1}^{m} \right.$$

$$\left. -\tfrac{1}{6}\ddot{d}_{j+1,n-1}^{m} - \tfrac{2}{3}\ddot{d}_{j+1,n}^{m} - \tfrac{1}{6}\ddot{d}_{j+1,n+1}^{m} \right) - \rho h \frac{\ell_4^2-\ell_1^2}{\ell_1^2} \left(-\tfrac{1}{6}\ddot{d}_{j-1,n-1}^{M} - \tfrac{2}{3}\ddot{d}_{j-1,n}^{M} - \tfrac{1}{6}\ddot{d}_{j-1,n+1}^{M} \right.$$

$$\left. +\tfrac{1}{3}\ddot{d}_{j,n-1}^{M} + \tfrac{4}{3}\ddot{d}_{j,n}^{M} + \tfrac{1}{3}\ddot{d}_{j,n+1}^{M} - \tfrac{1}{6}\ddot{d}_{j+1,n-1}^{M} - \tfrac{2}{3}\ddot{d}_{j+1,n}^{M} - \tfrac{1}{6}\ddot{d}_{j+1,n+1}^{M} \right)$$

$$+\frac{\Delta t^2}{4}\left(\frac{E}{h}+\frac{q^2}{\mu h}\right) \left(\ddot{d}_{j-1,n-1}^{m} - 2\ddot{d}_{j-1,n}^{m} + \ddot{d}_{j-1,n+1}^{m} + 2\ddot{d}_{j,n-1}^{m} - 4\ddot{d}_{j,n}^{m} + 2\ddot{d}_{j,n+1}^{m} \right.$$

$$\left. +\ddot{d}_{j+1,n-1}^{m} - 2\ddot{d}_{j+1,n}^{m} + \ddot{d}_{j+1,n+1}^{m} \right) \quad = \quad 0 \quad (37)$$

Substituting the trial solutions of Eqns. (32) then leads to

$$\frac{2}{3}\frac{\ell_4^2}{\ell_1^2}D^{m}\left(1-\cos(kc\Delta t)\right)\left(2+\cos(kh)\right) - \frac{2}{3}\frac{\ell_4^2-\ell_1^2}{\ell_1^2}D^{M}\left(1-\cos(kc\Delta t)\right)\left(2+\cos(kh)\right)$$

$$-\frac{c_{bar}^2\Delta t^2}{h^2}D^{m}\left(1+\cos(kc\Delta t)\right)\left(1-\cos(kh)\right) \quad = \quad 0 \quad (38)$$

Finally, eliminating the two amplitudes D^{m} and D^{M} from Eqns. (34) and (38) and resolving for the phase velocity c leads to the dispersion relation of the discrete equations:

$$\cos(kc\Delta t) = \frac{A_1 - A_2}{A_1 + A_2} \quad (39)$$

where

$$A_1 = \tfrac{2}{3}\left(2+\cos(kh)\right)^2 + \frac{4\ell_4^2}{h^2}\left(2+\cos(kh)\right)\left(1-\cos(kh)\right) \quad (40a)$$

$$A_2 = \frac{c_{bar}^2\Delta t^2}{h^2}\left(1-\cos(kh)\right)\left\{2+\cos(kh)+\frac{6\ell_1^2}{h^2}\left(1-\cos(kh)\right)\right\} \quad (40b)$$

The results of Eq. (39) are compared to Eq. (29) for a range of values of the element size h (normalised with respect to ℓ_1) and the time step Δt (normalised with respect to ℓ_1/c_{bar}) in Figure 2, whereby $\ell_4/\ell_1 = 2$. The cut-off wave number set by the spatial resolution is $k = 2\pi/h$. It can be verified that using smaller element sizes or smaller time steps, but not both, does not necessarily lead to improved accuracy.

11
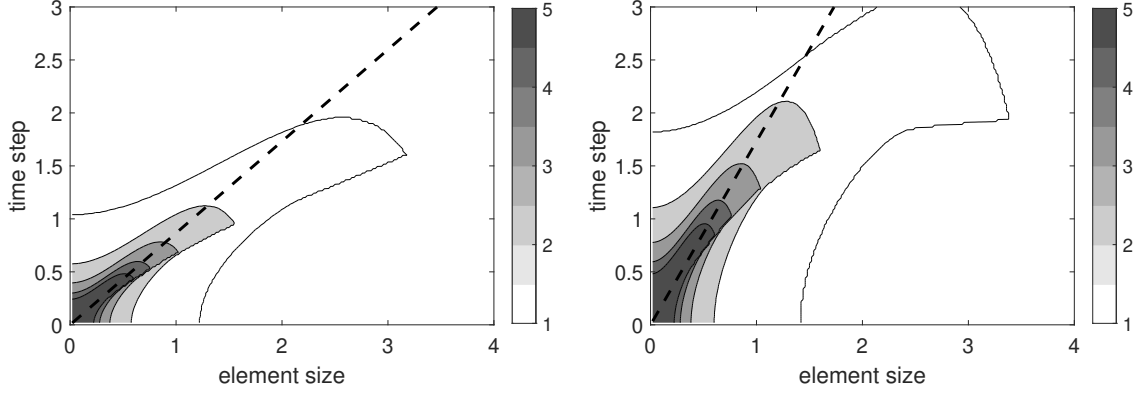
Figure 3: Discrete versus analytical dispersion curves: wave numbers captured with maximum 5% error for $\ell_4/\ell_1 = 1.5$ (left) and $\ell_4/\ell_1 = 3.0$ (right) — dashed lines indicate optimal time step estimates according to Eq. (47).

To provide a more holistic assessment of the influence of element size and time step on the accuracy, the discrepancy between the analytical dispersion curve of Eq. (29) and the numerical dispersion curve of Eq. (39) is evaluated by establishing the maximum wave number for which the difference between the two curves is no more than 5%. The results are plotted in Figure 3 for two length scale ratios ℓ_4/ℓ_1, and they confirm and quantify the findings of Figure 2: refinement of element size and refinement of time step must be balanced in order to maximise accuracy. For element sizes and time steps approaching zero, there appears to be an optimal ratio. This ratio is indicated with dashed lines in Figure 3 and will be quantified in the next Section.

6.3   Optimal ratio between time step and element size

It is possible to derive an analytical expression that verifies the observations made with respect to optimal ratio between time step and element size based on Figure 3. To do so, Eq. (39) is rewritten slightly as

$$1 - \cos(kc\Delta t) = 1 - \frac{A_1 - A_2}{A_1 + A_2} = \frac{2A_2}{A_1 + A_2} \tag{41}$$

Next, the two cosine functions are expanded into Taylor series as follows:

$$\cos(kc\Delta t) \approx 1 - \tfrac{1}{2}\left(kc\Delta t\right)^2 \tag{42a}$$

$$\cos(kh) \approx 1 - \tfrac{1}{2}\left(kh\right)^2 + \tfrac{1}{24}\left(kh\right)^4 \tag{42b}$$

That is, the time step function is expanded into a second-order series whereas the element size function is expanded into a fourth-order series. This difference is deliberate: the fourth-order expansion of the element size function is required for reasons of accuracy, whereas a fourth-order expansion of the time step function leads to much more complicated equations that do not improve insight compared to the second-order expansion.

Substituting the Taylor series expansions into Eqns. (40) and (41) yields

$$\frac{c^2}{c_{\text{bar}}^2} \approx \frac{B_1\left(B_2 + B_1\ell_1^2 k^2\right)}{B_2\left(B_2 + B_1\ell_4^2 k^2\right) + \tfrac{1}{4}c_{\text{bar}}^2\Delta t^2 k^2 B_1\left(B_2 + B_1\ell_1^2 k^2\right)} \tag{43}$$

where

$$B_1 = 1 - \tfrac{1}{12}h^2 k^2 \tag{44a}$$

$$B_2 = 1 - \tfrac{1}{6}h^2 k^2 + \tfrac{1}{72}h^4 k^4 \tag{44b}$$

12

Inspection of Figure 2 shows that the numerical dispersion curve deviates from the analytical dispersion curve for the higher wave numbers. Inspection of Eq. (29) shows that this behaviour is governed by the ratio ℓ_1/ℓ_4. Thus, the numerical dispersion curve can be brought closer to the analytical dispersion curve by matching the coefficients of the two length scales in the numerator and denominator of Eq. (43). These coefficients are

$$\text{numerator of Eq. (43):} \quad B_1^2\ell_1^2k^2 = \ell_1^2k^2\left(1 - \tfrac{1}{6}k^2h^2 + \tfrac{1}{144}k^4h^4\right) \tag{45a}$$

$$\text{denominator of Eq. (43):} \quad B_1B_2\ell_4^2k^2 + \tfrac{1}{4}c_{\text{bar}}^2\Delta t^2k^2 \cdot B_1^2\ell_1^2k^2 =$$
$$\ell_4^2k^2\left(1 - \tfrac{1}{4}k^2h^2 + \tfrac{1}{36}k^4h^4 - \tfrac{1}{864}k^6h^6\right)$$
$$+ \ell_1^2k^2 \cdot \tfrac{1}{4}c_{\text{bar}}^2\Delta t^2k^2\left(1 - \tfrac{1}{6}k^2h^2 + \tfrac{1}{144}k^4h^4\right) \tag{45b}$$

The terms proportional to k^2 are independent of Δt and match identically the corresponding values in Eq. (29). For the k^4-terms to match the ratio ℓ_1^2/ℓ_4^2, we require

$$\frac{-\tfrac{1}{6}\ell_1^2h^2}{-\tfrac{1}{4}\ell_4^2h^2 + \tfrac{1}{4}\ell_1^2c_{\text{bar}}^2\Delta t^2} = \frac{\ell_1^2}{\ell_4^2} \tag{46}$$

which can be solved for either Δt in terms of h, or vice versa. In particular, a time step that is optimal for accuracy can thus be expressed as

$$\Delta t \approx \frac{h}{c_{\text{bar}}\sqrt{3}} \cdot \frac{\ell_4}{\ell_1} \tag{47}$$

which is approximate as it ignores contributions of k^6 and higher. Despite the inexact nature of this solution, it can be verified from Figure 3 that it provides a reliable and accurate estimation of the best ratio between time step and element size.

7 Numerical results

The formulation of Section 5 has been implemented in one and two-dimensional finite element codes. For the time integration, the standard Newmark scheme with constant average acceleration has been used. Unless indicated otherwise, we have applied tyings between the (normal components of the) micro and macro-scale displacements on the boundaries [14]. Furthermore, the micro-scale magnetic potential of an arbitrary node is set equal to zero—this has no consequences for the evaluation of the usual engineering quantities of interest, i.e. the magnetic field $H_i = -\phi_{,i}$ and magnetic flux density $B_k = q_{ijk}\varepsilon_{ij} + \mu_{ik}H_i$, but it precludes rank deficiency of the third row of Eq. (21).

7.1 Convergence study

Eqns. (21) and (22) suggest that standard linear shape functions are sufficient for implementation. To demonstrate that this is an appropriate choice, a one-dimensional convergence study is carried out. An unsupported bar of length $L = 100$ m and unit cross-sectional area is subjected to a tensile load F with unit magnitude on its left end. The material constants are taken as $E = 3$ N/m^2, $q = 1$ N/Am, $\mu = 1$ Ns^2/C^2 and $\rho = 1$ kg/m^3. From Eq. (30) it follows that $c_{\text{bar}} = 2$ m/s. The length scale parameters are taken as $\ell_1 = 2$ m and $\ell_4 = 4$ m. This convergence study focusses on the solution of Eq. (21) which does not require ℓ_3.

Finite element meshes consisting of 10, 20, 40, 80, 160 and 320 finite elements have been used. The shape functions for all three fields (micro and macro-scale displacements, micro-scale magnetic potential) have been taken as linear. The solutions have been compared to a reference solution obtained from a mesh with 1280 linear finite elements. The comparison is based on the relative L_2-norm η of the error given by

$$\eta = \sqrt{\frac{\int\limits_V (\mathbf{s} - \mathbf{s}_{\text{ref}})^T (\mathbf{s} - \mathbf{s}_{\text{ref}}) \, \mathrm{d}\Omega}{\int\limits_V \mathbf{s}_{\text{ref}}^T\mathbf{s}_{\text{ref}} \, \mathrm{d}\Omega}} \tag{48}$$
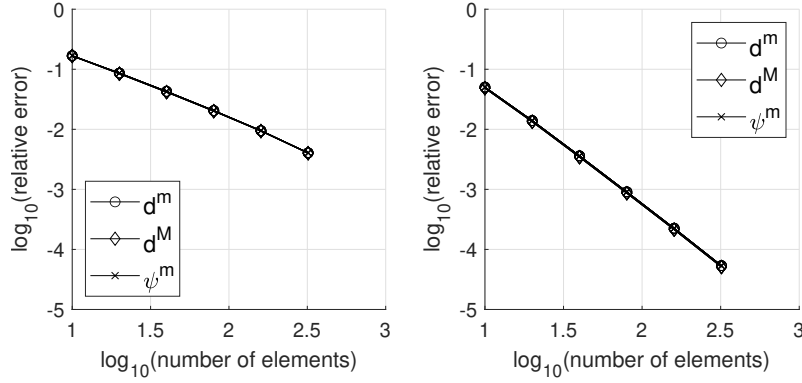
13

Figure 4: Relative error versus number of elements: Heaviside loading function (left) and trigonometric loading function (right)

where the solution **s** can be the micro-scale displacement, the macro-scale displacement, or the micro-scale magnetic potential. The time step is taken as $\Delta t = h\ell_4/2c_{\mathrm{bar}}\ell_1$, roughly in line with Eq. (47).

In addition, two loading functions have been used: a Heaviside function F_1 and a gradually evolving load F_2 according to

$$F_1(t) = \begin{cases} 0 & \text{for } t < 0 \\ 1 & \text{for } t \geq 0 \end{cases} \tag{49a}$$

$$F_2(t) = \frac{1}{2}\left(1 - \cos\frac{2\pi t}{t_{\mathrm{end}}}\right) \tag{49b}$$

with $t_{\mathrm{end}} = 25$ s. It is well-known [22,43] that the solutions of hyperbolic systems show similar convergence behaviour to those of elliptic systems, provided that the initial data are sufficiently smooth—in that context, F_1 and F_2 represent non-smooth and smooth loading functions, respectively. The results, evaluated at time $t = 25$ s, are plotted in Figure 4 against the number of elements in the standard double logarithmic scale.

It can be seen that taking the Heaviside loading function $F = F_1$ leads to suboptimal convergence rates: the relevant slopes in the top left and top right plots of Figure 4 are well below the theoretical rate of 2; in fact all slopes are virtually identical to 1. On the other hand, taking the trigonometric loading function $F = F_2$ leads to results for all three fields of primary unknowns that converge with the theoretical rate of 2. This provides evidence and assurance that the suggested finite element implementation is appropriate; it also suggests that the set of results for $F = F_1$ is dominated by the non-smooth initial conditions [43].

7.2 Wave dispersion

The ability of the model to simulate dispersive wave propagation is tested next. The same one-dimensional set-up is taken, with the same values for the material properties E, ρ, q and μ. An impact load is used, i.e. $F = F_1$ as given in Eq. (49a). Unless specified otherwise, the length scale parameters are given by $\ell_1 = 2$ m, $\ell_4/\ell_1 = 1.5$ and $\ell_3/\ell_1 = 1.5$. The number of elements is 160 and the time step is taken as $\Delta t = h/c_{\mathrm{bar}}$.

The distributions of micro-scale and macro-scale strain $\varepsilon = \partial u/\partial x$ and magnetic field $H = -\partial\phi/\partial x$ are plotted at different time instances in Figure 5. Note that the longitudinal coordinate on the horizontal axes has been adjusted with the product of bar speed and time, so that a zero horizontal coordinate corresponds with the position of the wave front in standard (i.e. non-gradient enriched) theory. It can be seen that the wave fronts of all four fields becomes less and less steep as time progresses. This is an indication that the harmonic components of higher frequency travel with lower velocity, and confirms that the model is dispersive—see [44] and Section 6.1 above. The micro-scale fields are more oscillatory than the associated macro-scale fields, which can be understood from the equivalence with homogenisation as explained in Section 2. An anomaly in all four fields is that the signal extends *ahead* of the wave front (infinitely far,
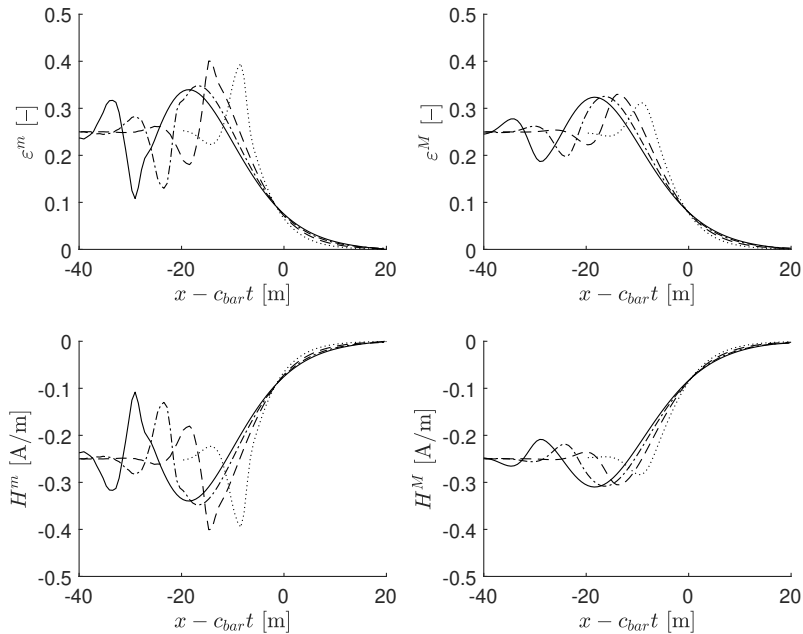
Figure 5: Dispersive wave propagation: micro-scale (left) and macro-scale (right) values of strain (top) and magnetic field (bottom) at times $t = 10$ s (dotted), $t = 20$ s (dashed), $t = 30$ s (dot-dashed) and $t = 40$ s (solid)

albeit with vanishing magnitude); it was shown by Metrikine that this lack of causality can be remedied by included higher-order time derivatives in the model [34], but this will not be pursued in the present study.

Next, the effect of the various length scales ℓ_1, ℓ_3 and ℓ_4 on the dispersive properties of the material is investigated in more detail. In [44] and in Section 6.1, we demonstrated that the ratio ℓ_4/ℓ_1 is the dominant parameter in this context, with higher wave numbers travelling slower for increased values of ℓ_4/ℓ_1. In Figure 6 we have plotted the results of micro-scale and macro-scale strain for two ratios of ℓ_4/ℓ_1. It can be verified that larger values of ℓ_4/ℓ_1 lead to a more rapid decrease of the slope of the wave front, which is consistent with higher wave numbers having a lower phase velocity.

However, it was also shown that taking $\ell_4/\ell_1 = 1$ leads to a non-dispersive model. With this set of parameters Eqns. (11a–11c) revert back to the classical piezomagnetic equations, whereby the effects of gradient enrichment are absent from the transient response. To verify this, we have taken $\ell_4^2/\ell_1^2 = 1.001$ which avoids rank deficiency of Eq. (21) but is otherwise sufficiently close to unity to demonstrate non-dispersive wave propagation. This is combined with different values for the third length scale of the model, i.e. ℓ_3. Figure 7 shows the results for the micro-scale and macro-scale magnetic field. It can be observed that the wave front for both fields maintains its slope for progressive time instants, which confirms the absence of dispersion. Although the macro-scale magnetic field is a smoothed version of the micro-scale magnetic field, this smoothing is a post-processing operation and does not feed back into the wave propagation—cf. the static equation (11d) which is decoupled from the transient system of equations (11a–11c). The length scale ℓ_3, associated with the homogenisation of the magnetic potential, therefore does not affect the dispersive properties of the model.

7.3   Removal of singularities

Finally, the ability of the model to remove singularities is tested. Indeed, this has been one of the main motivations in developing gradient theories [5, 10]. It was shown in [45] that the static model of Eqns. (6) is able to predict singularity-free strains for $\ell_1 > 0$ and singularity-free magnetic fields for $\ell_3 > 0$. However, since Eq. (8a) has been replaced by its acceleration equivalent Eq. (11b), it is pertinent to verify
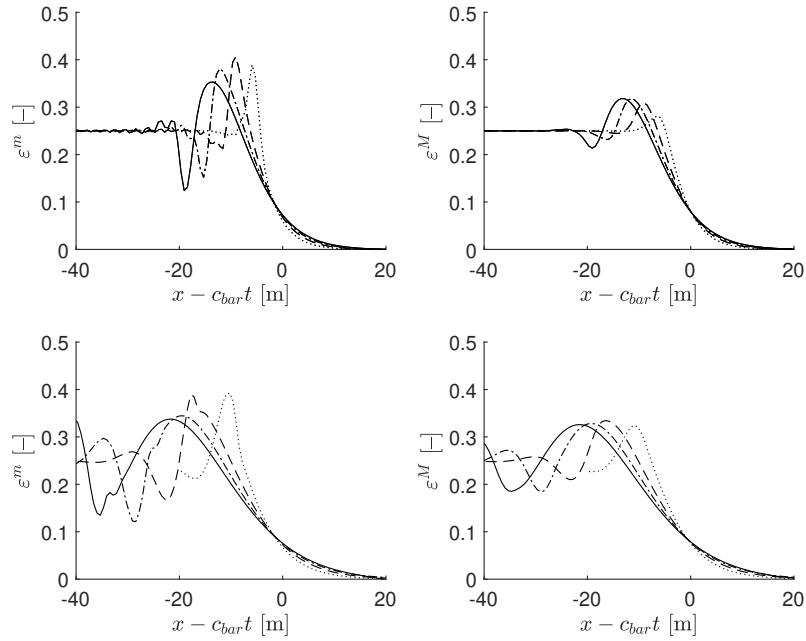
15

Figure 6: Dispersive wave propagation: micro-scale strain (left) and macro-scale strain (right) for $\ell_4^2/\ell_1^2 = 1.5$ (top) and $\ell_4^2/\ell_1^2 = 3$ (bottom) at times $t = 10$ s (dotted), $t = 20$ s (dashed), $t = 30$ s (dot-dashed) and $t = 40$ s (solid)
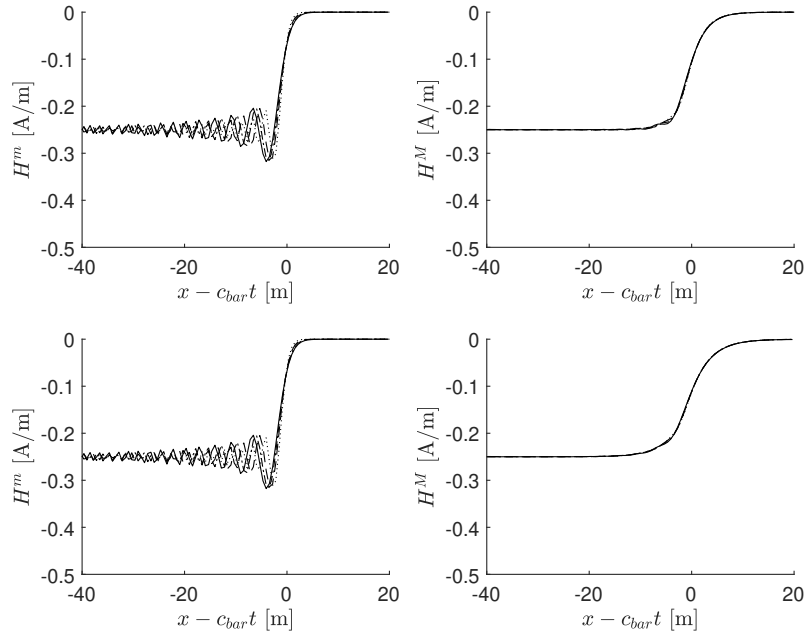

Figure 7: Non-dispersive wave propagation: micro-scale magnetic field (left) and macro-scale magnetic field (right) for $\ell_3^2/\ell_1^2 = 1.5$ (top) and $\ell_3^2/\ell_1^2 = 3$ (bottom) at times $t = 10$ s (dotted), $t = 20$ s (dashed), $t = 30$ s (dot-dashed) and $t = 40$ s (solid)

the performance of the new model.

To do so, we will study the two two-dimensional geometries given in Figure 8, where thin lines on
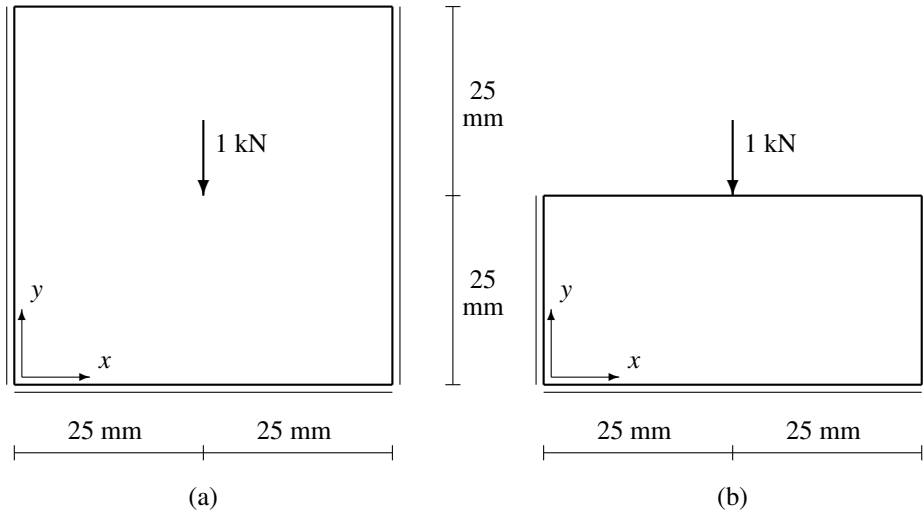
Figure 8: Geometries to study singularity removal: force applied on interior of the domain (a) and on free boundary (b)

the boundaries indicate that the normal components of the displacement are fixed. Concentrated forces are applied on the interior of the domain or on a free boundary; in a classical continuum theory such forces would locally lead to singularities. A plane stress configuration is assumed, and the material properties are those of a transversely isotropic magnetostrictive Terfenol-D/epoxy composite. In terms of the relevant material properties of Eqns. (18), we have adopted the values from [20, 31] given by

$$\mathbf{C} = \begin{bmatrix} 31.1 & 15.2 & 0 \\ 15.2 & 35.6 & 0 \\ 0 & 0 & 13.6 \end{bmatrix} \cdot 10^3 \ \text{N/mm}^2 \tag{50a}$$

$$\mathbf{Q} = \begin{bmatrix} 0 & 156.8 \\ 0 & 108.3 \\ -60.9 & 0 \end{bmatrix} \cdot 10^{-3} \ \text{N/Amm} \tag{50b}$$

$$\mathbf{P} = \begin{bmatrix} 5.4 & 0 \\ 0 & 5.4 \end{bmatrix} \cdot 10^{-6} \ \text{Ns}^2/\text{C}^2 \tag{50c}$$

while the mass density $\rho = 9.2 \cdot 10^{-9}$ Ns^2/mm^4. Furthermore, the internal length parameters are taken as $\ell_1^2 = 4$ mm^2 and $\ell_3^2 = \ell_4^2 = 4.8$ mm^2—the latter values are not meant to represent grain sizes, but merely to test the ability of the model to remove singularities. Structured meshes with bilinear quadrilateral finite elements are used with 16, 32 and 64 square elements in the x-direction. Time integration is carried out until time $t = 1.6 \cdot 10^{-5}$ s with time step $\Delta t = 2.56 \cdot 10^{-7} h$ s where h is the element size.

First, the geometry of Figure 8 (a) is studied. Since in this configuration the force is applied in the interior of the domain, any presence or absence of a singularity is caused by the field equations alone, not by the boundary conditions. In Figure 9 the micro and macro-scale normal strains ε_{yy} as well as the micro and macro-scale magnetic field H_y are plotted at the end of the analysis along the bottom half of the vertical symmetry axis. It is clear that the macro-scale fields converge to a unique, finite solution and, thus, that singularities have been removed from the macro-scale fields. On the other hand, both micro-scale fields exhibit peak values that are an order of magnitude large than the macro-scale ones. Moreover, these microscale peak values appear to grow unbounded with a decreasing element size. In other words, these fields do not converge to a finite solution and still contain singularities. Since in this geometry the appearance of singularities is not affected by the boundary conditions, the conclusion is that the field equations (11) are capable of removing singularities from the macro-scale fields, but not from the micro-scale fields.
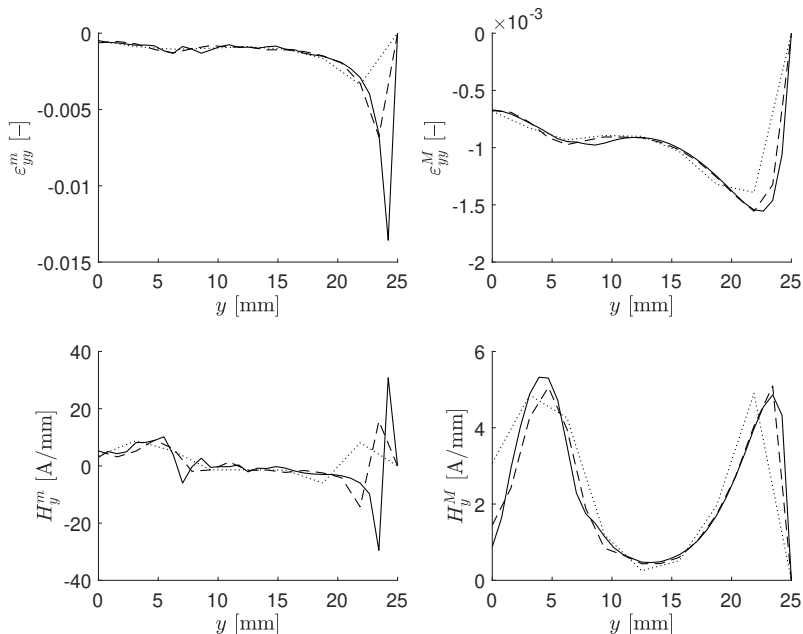
17

Figure 9: Singularity removal: geometry of Figure 8 (a), micro-scale (left) and macro-scale (right) profiles of strain (top) and magnetic field (bottom). Line types refer to 16 (dotted), 32 (dashed) and 64 (solid) elements in *x*-direction.

Next, the geometry of Figure 8 (b) is considered. The position of a potential singularity now coincides with the boundary, thus it is of interest to establish the role of the boundary conditions in the suppression (or otherwise) of singularities. In particular, the effect of tyings between the micro and macro-scale displacement will be studied. Tyings have been suggested in a gradient elasticity context using arguments of volume preservation and avoidance of boundary layers [10, 14], but it was also found that tyings could prohibit the ability of a model to suppress singularities [10]. Here, we will verify these effects in a gradient-enriched piezomagnetic framework.

Figures 10 and 11 show the results with and without tyings, respectively, between the normal components of the micro and macro-scale displacements. Similar to the simulations with the full geometry, cf. Figure 9, the micro-scale strain and magnetic field appear to grow unbounded upon mesh refinement, which is an indication for the presence of singularities—this holds for the case with and without tyings. On the other hand, the macro-scale magnetic field converges to a unique, finite solution, irrespective of whether or not tyings are applied. The reason is that Eq. (26) is solved separately from Eq. (23), and is thus not affected by the imposition or otherwise of tyings between micro and macro-scale displacements. The only field affected by the tyings is the macro-scale strain. Figure 10 shows this field grows unbounded upon mesh refinement in case tyings are present. This, again, is an indication that the strain is singular, and this singularity must be attributed to the boundary conditions, since in Figure 9 we have demonstrated that the field equations are capable of removing singularities. Conversely, removing tyings between the two displacement fields leads to a macro-scale strain that converges to a unique, finite solution—see Figure 11.

8 Conclusions

In this paper, we have formulated and implemented a gradient-enriched dynamic piezomagnetic model. The enrichment with higher-order spatial gradients of the displacements and the magnetic potential introduces microstructural effects into the model that can be used to model dispersive wave propagation and to remove singularities from the simulated response. Specific observations are as follows.
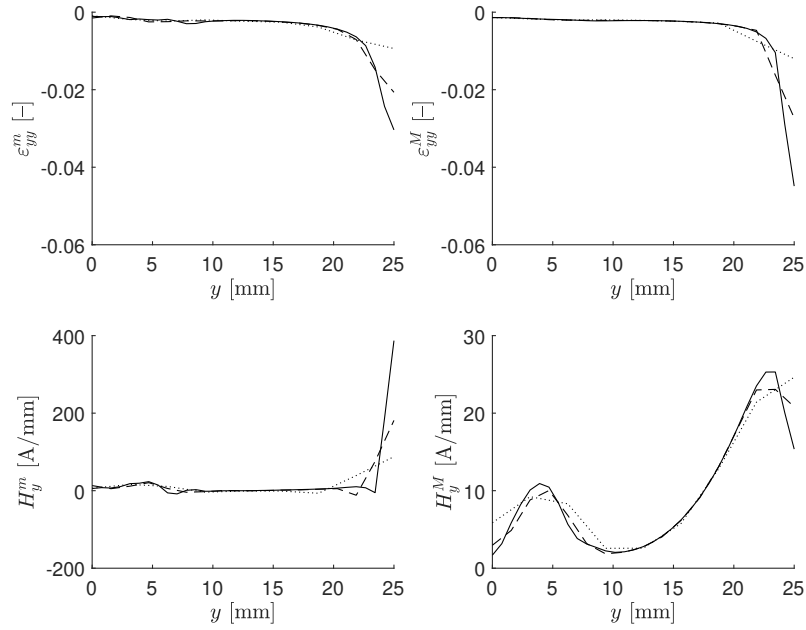
18

Figure 10: Singularity removal: geometry of Figure 8 (b) with tyings, micro-scale (left) and macro-scale (right) profiles of strain (top) and magnetic field (bottom). Line types refer to 16 (dotted), 32 (dashed) and 64 (solid) elements in *x*-direction.
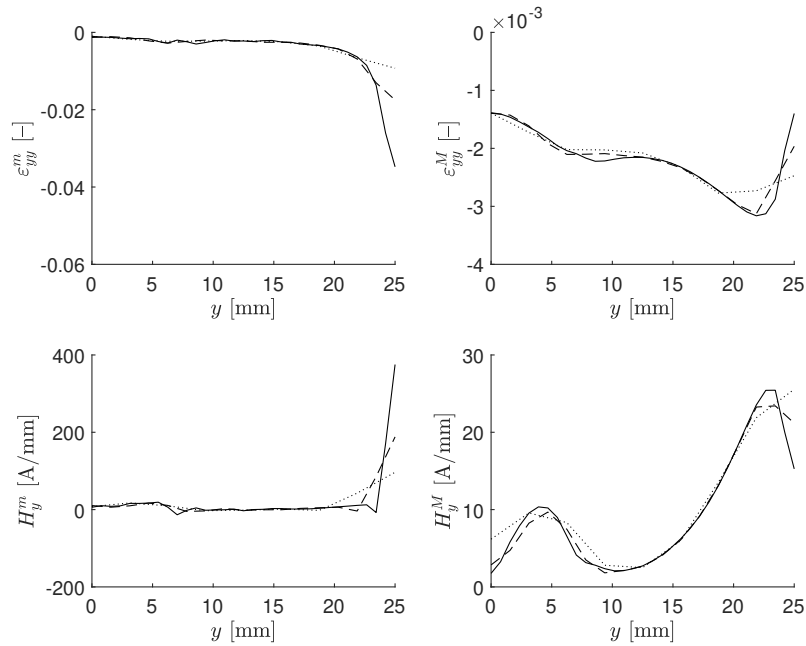

Figure 11: Singularity removal: geometry of Figure 8 (b) without tyings, micro-scale (left) and macro-scale (right) profiles of strain (top) and magnetic field (bottom). Line types refer to 16 (dotted), 32 (dashed) and 64 (solid) elements in *x*-direction.

- In our model, we have only accounted for transient mechanical terms and ignored transient magnetic terms, given the very large difference in magnitude between the propagation velocities of mechanical

and magnetic signals.

- The higher-order terms of the model that appeared due to the gradient enrichment have been rewritten in multi-scale terms, using principles of homogenisation. The result is a multi-scale model in which micro-scale displacements and magnetic potentials are included alongside their macro-scale counterparts.

- Thermodynamic consistency is demonstrated through a parallel derivation of the model from a multi-scale energy functional, together with the variationally consistent boundary conditions.

- As a consequence of the multi-scale reformulation of the equations, the highest order of (spatial) derivation in the model reduces from four to two. This greatly facilitates finite element implementation. We have presented the relevant finite element equations and verified that convergence upon mesh refinement corresponds to theoretically predicted rates.

- Based on a comparison between the dispersive properties of the continuum equations and the discretised equations, we have derived an optimal ratio between the time step and the element size.

- The model is able to predict dispersive wave propagation. The parameter that controls the dispersive properties is the ratio of the length scales related to acceleration and strain.

- The model is able to predict macro-scale fields that are free of singularities, provided that appropriate boundary conditions are selected. Singularities remain in the associated micro-scale fields. Thus, predictions of structural or material integrity must be based on the macro-scale fields, not the micro-scale fields.

Acknowledgements

A Newmark equations

The Newmark time integration equations relating time step j to time step $j+1$ for a generic variable s read

$$\dot{s}_{j+1} = \dot{s}_j + (1-\gamma)\,\Delta t\,\ddot{s}_j + \gamma\Delta t\,\ddot{s}_{j+1} \tag{51a}$$

$$s_{j+1} = s_j + \Delta t\dot{s}_j + \left(\tfrac{1}{2}-\beta\right)\Delta t^2\ddot{s}_j + \beta\Delta t^2\ddot{s}_{j+1} \tag{51b}$$

whereas the equations relating time step $j-1$ to time step j are given by

$$\dot{s}_j = \dot{s}_{j-1} + (1-\gamma)\,\Delta t\,\ddot{s}_{j-1} + \gamma\Delta t\,\ddot{s}_j \tag{52a}$$

$$s_j = s_{j-1} + \Delta t\dot{s}_{j-1} + \left(\tfrac{1}{2}-\beta\right)\Delta t^2\ddot{s}_{j-1} + \beta\Delta t^2\ddot{s}_j \tag{52b}$$

Here, β and γ are user-defined parameters that can be set to control the numerical damping, stability and accuracy of the method. Subtracting Eq. (52b) from Eq. (51b) gives

$$\begin{aligned}
s_{j-1} - 2s_j + s_{j+1} &= \Delta t\left(\dot{s}_j - \dot{s}_{j-1}\right) - \left(\tfrac{1}{2}-\beta\right)\Delta t^2\ddot{s}_{j-1} + \left(\tfrac{1}{2}-2\beta\right)\Delta t^2\ddot{s}_j + \beta\Delta t^2\ddot{s}_{j+1} \\
&= \left(\tfrac{1}{2}-\gamma+\beta\right)\Delta t^2\ddot{s}_{j-1} + \left(\tfrac{1}{2}+\gamma-2\beta\right)\Delta t^2\ddot{s}_j + \beta\Delta t^2\ddot{s}_{j+1}
\end{aligned} \tag{53}$$

where Eq. (52a) is used to eliminate the velocities. The constant average acceleration method is obtained by taking $\gamma = \frac{1}{2}$ and $\beta = \frac{1}{4}$, in which case

$$s_{j-1} - 2s_j + s_{j+1} = \tfrac{1}{4}\Delta t^2 \left(\ddot{s}_{j-1} + 2\ddot{s}_j + \ddot{s}_{j+1} \right) \tag{54}$$

which allows to rewrite displacements in terms of accelerations, or vice versa.

References

[1] J. Aboudi. Field distributions in cracked periodically layered electromagnetothermoelastic composites. *J. Intell. Mater. Syst. Struct.*, 24:381–398, 2012.

[2] J. Aboudi. Multiscale analysis for the prediction of the full field in electromagnetoelastic composites with semi-infinite cracks. *J. Intell. Mater. Syst. Struct.*, 28:1734–1750, 2017.

[3] E.C. Aifantis. On the microstructural origin of certain inelastic models. *ASME J. Engng. Mater. Techn.*, 106:326–330, 1984.

[4] E.C. Aifantis. The physics of plastic deformation. *Int. J. Plast.*, 3:211–247, 1987.

[5] E.C. Aifantis. On the role of gradients in the localization of deformation and fracture. *Int. J. Engng. Sci.*, 30:1279–1299, 1992.

[6] M. Arefi and M. Kiani. Magneto-electro-mechanical bending analysis of three-layered exponentially graded microplate with piezomagnetic face-sheets resting on Pasternak's foundation via MCST. *Mech. Adv. Mater. Struct.*, 27:383–395, 2020.

[7] M. Arefi, M. Kiani, and T. Rabczuk. Application of nonlocal strain gradient theory to size dependent bending analysis of a sandwich porous nanoplate integrated with piezomagnetic face-sheets. *Compos. B*, 168:320–333, 2019.

[8] M. Arefi, M. Kiani, and A.M. Zenkour. Size-dependent free vibration analysis of a three-layered exponentially graded nano-/micro-plate with piezomagnetic face sheets resting on Pasternak's foundation via MCST. *J. Sandw. Struct. Mater.*, 22:55–86, 2020.

[9] M. Arefi, M.H. Zamani, and M. Kiani. Smart electrical and magnetic stability analysis of exponentially graded shear deformable three-layered nanoplate based on nonlocal piezo-magneto-elasticity theory. *J. Sandw. Struct. Mater.*, 22:599–625, 2020.

[10] H. Askes and E.C. Aifantis. Gradient elasticity in statics and dynamics: An overview of formulations, length scale identification procedures, finite element implementations and new results. *Int. J. Solids Struct.*, 48:1962–1990, 2011.

[11] H. Askes, T. Bennett, and E.C. Aifantis. A new formulation and C^0-implementation of dynamically consistent gradient elasticity. *Int. J. Numer. Methods Engng.*, 72:111–126, 2007.

[12] H. Askes, D. De Domenico, M. Xu, I.M. Gitman, T. Bennett, and E.C. Aifantis. Operator splits and multiscale methods in computational dynamics. In A. Berezovski and T. Soomere, editors, *Applied Wave Mathematics II*, pages 239–255. Springer, 2019.

[13] H. Askes and I.M. Gitman. Reducible and irreducible forms of stabilised gradient elasticity in dynamics. *Math. Mech. Complex Syst.*, 5:1–17, 2017.

[14] H. Askes, A.V. Metrikine, A.V. Pichugin, and T. Bennett. Four simplified gradient elasticity models for the simulation of dispersive wave propagation. *Phil. Magaz.*, 88:3415–3443, 2008.

[15] H. Askes, I. Morata, and E.C. Aifantis. Finite element analysis with staggered gradient elasticity. *Comput. Struct.*, 86:1266–1279, 2008.

[16] T. Bennett and H. Askes. Finite element modelling of wave dispersion with dynamically consistent gradient elasticity. *Comput. Mech.*, 43:815–825, 2009.

[17] T. Bennett, A. Rodríguez-Ferran, and H. Askes. Damage regularisation with inertia gradients. *Eur. J. Mech. A/Solids*, 31:131–138, 2012.

[18] C. Bormio-Nunes and O. Hubert. Piezomagnetic behavior of Fe-Al-B alloys. *J. Magnetism Magn. Mater.*, 393:404–418, 2015.

[19] A.L. Chen, D.J. Yan, Y.S. Wang, and C. Zhang. In-plane elastic wave propagation in nanoscale periodic piezoelectric/piezomagnetic laminates. *Int. J. Mech. Sci.*, 153–154:416–429, 2019.

[20] A. Daga, N. Ganesan, and K. Shankar. Comparative studies of the transient response for PECP, MSCP, Barium Titanate, magneto-electro-elastic finite cylindrical shell under constant internal pressure using finite element method. *Finite Elem. Anal. Des.*, 44:89–104, 2008.

[21] D. De Domenico and H. Askes. Computational aspects of a new multi-scale dispersive gradient elasticity model with micro-inertia. *Int. J. Numer. Methods Engng*, 109:52—72, 2016.

[22] T. Dupont. L^2-estimates for Galerkin methods for second order hyperbolic equations. *SIAM J. Numer. Analysis*, 10:880–889, 1973.

[23] A.C. Eringen. On differential equations of nonlocal elasticity and solutions of screw dislocation and surface waves. *J. Appl. Phys.*, 54:4703–4710, 1983.

[24] R. Gholami, R. Ansari, and Y. Gholami. Size-dependent bending, buckling and vibration of higher-order shear deformable magneto-electro-thermo-elastic rectangular nanoplates. *Mater. Res. Express*, 4:065702, 2017.

[25] I.M. Gitman, H. Askes, and E.C. Aifantis. The representative volume size in static and dynamic micro-macro transitions. *Int. J. Fract.*, 135:L3–L9, 2005.

[26] U. Güven. Transverse vibrations of single-walled carbon nanotubes with initial stress under magnetic field. *Compos. Struct.*, 114:92–98, 2014.

[27] O. Hubert. Multiscale magneto-elastic modeling of magnetic materials including isotropic second order stress effect. *J. Magnetism Magn. Mater.*, 491:165564, 2019.

[28] O. Hubert and L. Daniel. Multiscale modeling of the magneto-mechanical behavior of grain-oriented silicon steels. *J. Magnetism Magn. Mater.*, 320:1412–1422, 2008.

[29] A. Jamalpoor and M. Hosseini. Biaxial buckling analysis of double-orthotropic microplate-systems including in-plane magnetic field based on strain gradient theory. *Compos. B Engng.*, 75:53–64, 2015.

[30] V.G. Kouznetsova, M.G.D. Geers, and W.A.M. Brekelmans. Size of a Representative Volume Element in a second-order computational homogenization framework. *Int. J. Multiscale Comput. Engng.*, 2:575–598, 2004.

[31] Y.X. Liu, J.G. Wan, J.M. Liu, and C.W. Nan. Effect of magnetic bias field on magnetoelectric coupling in magnetoelectric composites. *J. Appl. Phys.*, 94:5118–5122, 2003.

[32] S. Lurie, P. Belov, D. Volkov-Bogorodsky, and N. Tuchkova. Nanomechanical modeling of nanostructures and dispersed composites. *Comput. Mater. Sci.*, 28:529–539, 2003.

[33] M. Malikan, V.B. Nguyen, and F. Tornabene. Electromagnetic forced vibrations of composite nanoplates using nonlocal strain gradient theory. *Mater. Res. Express*, 5:075031, 2018.

[34] A.V. Metrikine. On causality of the gradient elasticity models. *J. Sound Vibr.*, 297:727–742, 2006.

[35] K.B. Mustapha and D. Ruan. Size-dependent axial dynamics of magnetically-sensitive strain gradient microbars with end attachments. *Int. J. Mech. Sci.*, 94–95:96–110, 2015.

[36] S. Narendar, S.S. Gupta, and S. Gopalakrishnan. Longitudinal magnetic field effect on nonlocal ultrasonic vibration analysis of single-walled carbon nanotubes based on wave propagation approach. *Adv. Sci. Letters*, 4:3382–3389, 2011.

[37] W.T. Park and S.C. Han. Buckling analysis of nano-scale magneto-electro-elastic plates using the nonlocal elasticity theory. *Adv. Mech. Engng.*, 10:1–16, 2018.

[38] R.H.J. Peerlings, R. de Borst, W.A.M. Brekelmans, and J.H.V. de Vree. Gradient enhanced damage for quasi-brittle materials. *Int. J. Numer. Meth. Engng.*, 39:3391–3403, 1996.

[39] C.Q. Ru and E.C. Aifantis. A simple approach to solve boundary-value problems in gradient elasticity. *Acta Mech.*, 101:59–68, 1993.

[40] L. Susmel, H. Askes, T. Bennett, and D. Taylor. Theory of Critical Distances versus Gradient Mechanics in modelling the transition from the short to long crack regime at the fatigue limit. *Fatigue Fract. Engng. Mater. Struct.*, 36:861–869, 2013.

[41] L.T. Tenek and E.C. Aifantis. A two-dimensional finite element implementation of a special form of gradient elasticity. *Comput. Model. Engng. Sci.*, 3:731–741, 2002.

[42] R.A. Toupin. Theories of elasticity with couple-stress. *Arch. Rat. Mech. Anal.*, 17:85–112, 1964.

[43] S.R. Wu. A priori error estimates for explicit finite element for linear elasto-dynamics by Galerkin method and central difference method. *Comput. Methods Appl. Mech. Engng.*, 192:5329–5353, 2003.

[44] M. Xu, H. Askes, and I.M. Gitman. Mono-scale and multi-scale formulations of gradient-enriched dynamic piezomagnetics. *Wave Mot.*, 91:102402, 2019.

[45] M. Xu, I.M. Gitman, and H. Askes. A gradient-enriched continuum model for magneto-elastic coupling: Formulation, finite element implementation and in-plane problems. *Comput. Struct.*, 212:275–288, 2019.

[46] Y.M. Yue, K.Y. Xu, and E.C. Aifantis. Microscale size effects on the electromechanical coupling in piezoelectric material for anti-plane problem. *Smart Mater. Struct.*, 23:125043, 2014.